Hardening Low-Carbon Steels by Engineering the Size and Distribution of Inclusions

HUIGAI LI, LIUXING WANG, HAITAO XIAO, JIALI XU, SHAOBO ZHENG, QIJIE ZHAI, and KE HAN

Ultra-hard low-carbon steels usually need many processing steps after casting. This paper introduces a single-step direct-cast hardening (DiCH) method for making ultra-hard, low-carbon steels by manipulating two variables: free oxygen content before solidification and cooling rate during solidification. Without any post-casting steps required to enhance hardness, DiCH produced property-gradient steel with high surface hardness (4.2 GPa Vickers) directly from liquid metal. The optimum size, number, and distribution of oxide inclusions were achieved in condition of intermediate oxygen content (25 to 45 ppm) and high cooling rate (≥ 550K/s). Ultra-high hardness was achieved at the surface of DiCH samples with a mixture of refined acicular ferrite (AF) and martensite-like ferrite (MF). Two factors contributed to refinement of microstructure and enhancement of hardness: a high cooling rate during the solidification process, and a high density of submicron oxide inclusions in the cast steel. At cooling rates higher than 2500 K/s, refined AF and MF was obtained, accompanied by high densities (up to 600/mm^2) of multiple-component, Ti-containing oxides of sizes between 0.5 and 0.7 μm.

https://doi.org/10.1007/s11661-018-5003-7

I. INTRODUCTION

LOW-CARBON steels, which are commonly used in machinery and engineering, such as automotive body panels, in general are considered valuable for their high toughness and ductility, but their hardness and strength are generally low.

In general, the strength and hardness of low-carbon steel varies according to: (1) the alloy content of the steel matrix, (2) the degree of reduction that occurs during hot-rolling, (3) the temperature during coiling, and (4) the duration/degree of heat treatment.[1–3] Yield strength can vary from 325 to 666 MPa (with alloying addition to enhance the hardenability), and the Vickers hardness values can reach as high as 263 Hv in some cases.[3] In low-carbon weld steel composed of AF, however, the average Vickers hardness value is 317 Hv.[4]

To enhance the surface hardness and maintain high toughness, surface treatment can be introduced. This will, however, increase the complexity of the process and an extra cost of production.

High hardness can also be achieved in some low-carbon steels by quenching. This converts austenite phase into martensite, whose Vickers hardness values reach 300 Hv in plain carbon steels with carbon content up to 0.1 pct.[5,6] In combination of alloy addition and quenching process, the Vickers hardness values reach 350[7] and 440 Hv.[8] Unfortunately, such high hardness in these steels comes at the cost of introducing an unnecessarily complex processing procedure and reducing toughness and ductility in the end product.

The above issues can be tackled in steels whose inclusions have been properly engineered. The distribution of oxide inclusions depends on the interaction between two variables: free oxygen content before solidification and cooling rate during solidification.[9–11] Higher free oxygen content in molten steel results in a low density of large, coarse oxides. Rapid cooling rate during solidification, on the other hand, results in greater undercooling, which provides a greater driving force for nucleation,[12] thus increasing the density of fine oxides. When these two variables are properly balanced, the result is an even distribution of fine oxides throughout the steel.

Oxide inclusions in steel are usually considered defects because, under most circumstances, the presence of inclusions causes cracking simply by interrupting the

HUIGAI LI, LIUXING WANG, HAITAO XIAO, JIALI XU, SHAOBO ZHENG, and QIJIE ZHAI are with the State Key Laboratory of Advanced Special Steel & Shanghai Key Laboratory of Advanced Ferrometallurgy & School of Materials Science and Engineering, Shanghai University, Shanghai 200444, China. Contact e-mail: lihuigai@i.shu.edu.cn KE HAN is with the National High Magnetic Field Laboratory, Florida State University, Tallahassee, 32310.

Manuscript submitted March 12, 2018.

Published online: 07 November 2018

continuity of the underlying grain structure of steel. Thus, oxygen content in steel is usually kept very low to avoid inclusions. Over time, however, metallurgists have discovered that the hardness of steel can actually be improved by certain types of inclusions. Consequently, designers of new steels may choose to introduce a higher initial oxygen content into the melt. They then manage the resulting oxide inclusions to ensure that these are very fine, dense, and evenly distributed. This occurs when steel solidifies rapidly, at cooling rates as high as, say, 10^2 to 10^3K/s.[13–15] Rapid cooling rates force large numbers of oxide inclusions to nucleate simultaneously, only to be immediately trapped, while they are still small, in the rapidly advancing solid/liquid interface, thus enhancing hardness without causing cracking.

Under certain circumstances, these fine inclusions can serve as nucleation sites for the formation of acicular ferrite (AF, Appendix II). If fine inclusions are not available, ferrite will instead nucleate on grain boundaries, producing polygonal ferrite (PF, Appendix II) or quasi-polygonal ferrite (Q-PF, Appendix II).[16,17] AF, on the other hand, is a phase involving needle-shaped grains in a chaotic arrangement that significantly increases the hardness and strength of steel,[18] unlike either PF or Q-PF, which have no such effect.

Oxide inclusions, regardless of their number and density, vary also in composition. It has been reported that Ti-containing inclusions, such as $MnTiO_3$, Ti_2O_3, and Ti-Mn-Si-O-S complex inclusions, provide much better sites for AF nucleation than, say, Al-containing inclusions.[19–21] The critical size for heterogeneous nuclei of AF varies from 0.3 to 7 μm, depending on the composition of oxide inclusions and the carbon content of the steel matrix.[22–25] When the number of Ti-containing inclusions increases, the amount of AF increases correspondingly.[26,27]

By combination of engineering the inclusion distribution and cooling rate, ultra-hard low-carbon steel was produced using the direct-cast hardening (DiCH) method. The steel has the same toughness and ductility of other steels produced using the ordinary process, and it has much higher surface hardness. Using DiCH, the Vickers hardness of the surface zone can reach twice as high as that of the interior. Surface examination indicated no embrittlement at the hardened region. This method avoids the expense of such extra processing as alloying, hot-rolling, cold-rolling, heat treatment, and surface treatment. We believe that the materials manufactured by DiCH could be valuable for use in appliances, cars, and any other devices that require panels with very high surface hardness.

II. MATERIALS AND METHODS

Ultra-hard low-carbon steel was produced through DiCH and compared to similar low-carbon steel of ordinary hardness. Three free oxygen levels (low, medium, and high) were used in the smelting process. Manganese, silicon, and titanium were added to the melt to form oxide inclusions. Two parameters were controlled: free oxygen content and cooling rate.

A. *Materials Preparation*

Four samples (S1 to S4) were prepared in the following manner. First, three separate batches (B1 to B3) of 5.81 kg TG30 steel were heated to 1600 °C in an

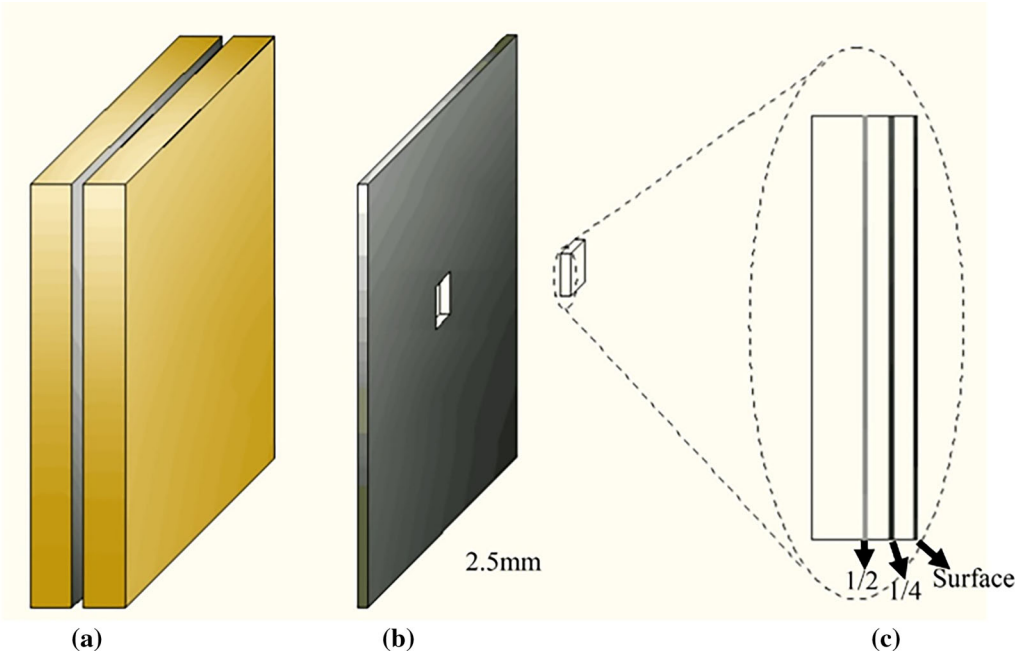

Fig. 1—Schematic illustration of copper plates and sample. (*a*) Pair of copper plates, each 5 to 9 mm thick. Thickness is different for different cooling rates. (*b*) Strip sample, 2.5 mm thick, formed in the space between the copper plates. (*c*) Inset showing cross section of sample, with the three study zones indicated by arrows.

induction furnace under 200 Pa air pressure. FeO was then added in order to raise the free oxygen content ($[O]_s$) in each batch to one of three levels: approximately 80 ppm for B1, approximately 25 ppm for B2, and approximately 40 ppm for B3. The temperature and $[O]_s$ were measured by a Heraeus high-precision disposable immersion sensor with an error of ± 5 °C.

The first batch (B1) was subjected to sequential addition of 20 g of 80 wt pct Mn Ferromanganese (FeMn) alloy and 6 g of 75 wt pct Si Ferrosilicon (FeSi) alloy. This batch was used to produce S1.

The second batch (B2) was subjected to a more complicated procedure. First, 57 g of FeMn and 19 g of FeSi were added sequentially. Following that, some of this melt was suctioned off and used to make S2. Then 4 g of 40 wt pct Ti Ferrotitanium (FeTi) (with an effective yield of 80 pct) alloy was added to the remaining melt, and this part was used to make S3.

The third batch (B3) was subjected to sequential addition of the following elements: 4 g of FeTi, 57 g of FeMn, and 19 g of FeSi. This batch was used to produce S4.

Each of the four samples was prepared by suctioning the melt into the space between two copper plates separated by 2.5 mm (see Figures 1(a) and (b)). Each pair of plates had been milled to the specifications necessary to produce the appropriate cooling rate for the sample. After hardening, the percent weight of major elements in the sample (Si, Mn, and Ti) was analyzed using an optical emission spectrometer (PMI-MASTER) with an error of ± 0.01 wt pct. Sample compositions are listed in Table I.

Table I. Chemical Composition of Each Sample (Weight Percent)

Sample	$[O]_s$	Si	Mn	Ti	C	Fe
S1	0.0068	0.08	0.28	< 0.002	0.03	balance
S2	0.0028	0.25	0.78			
S3	0.0011			0.02		
S4	0.0037					

B. *Cooling Rate Calculation*

Cooling rate varies with the thickness of the copper plates forming the mold—the thicker the plates, the higher the rate. More importantly, however, cooling rate slows considerably from surface to center within the sample. The cooling rate within the sample strongly affects the segregation of oxygen and thus the distribution of inclusions. Plate thickness, on the other hand, strongly affects the total number of inclusions but not necessarily their distribution.

The average cooling rate during phase transformation was calculated based on secondary dendrite arm spacing, measured separately in each sample (see Figure 2). For this calculation, strips measuring $10 \times 5 \times 2.5$ mm^3 were cut from the sample, polished, and thermal etched in supersaturated glacial acetic acid solution. They were then examined using a DM6000M light microscope. From 15 images, which were taken from 15 different areas, secondary dendrite arm spacing was measured by truncation method at the 1/4 depth of each sample. Each area was measured 3 to 5 times. The average values were calculated using all these data. The cooling rate was calculated by the secondary dendrite arm spacing equation[28]:

$$d = 688(60 \times R)^{-0.36} \quad [1]$$

where R is the cooling rate in K/s and d is the secondary dendrite arm spacing in μm. The average cooling rates at the 1/4 depth of S1, S2, S3, and S4 were 1200, 550, 150, and 2500 K/s, respectively, which were considered to be the cooling rates of the four samples in the following sections.

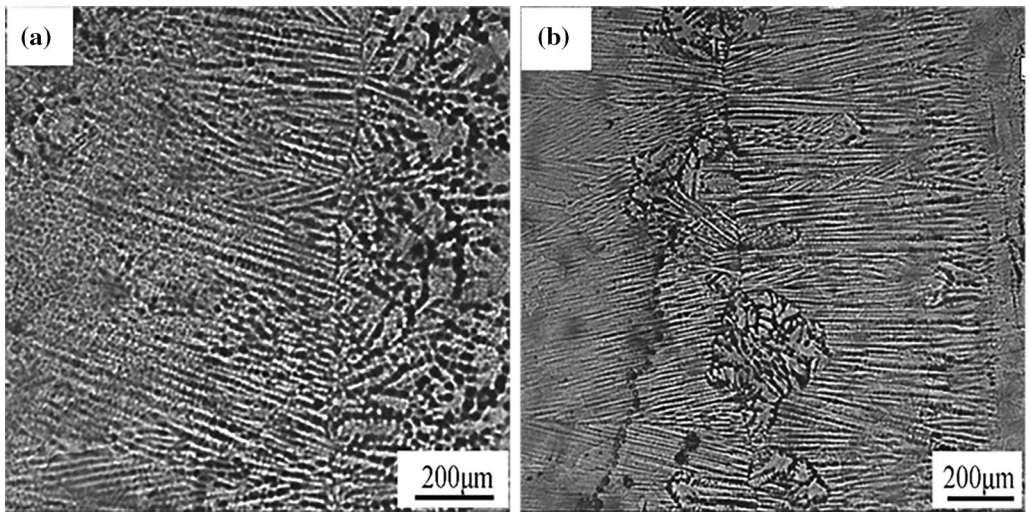

Fig. 2—Dendrite structure shown in cross section. (*a*) Dendrite structure of S1. (*b*) Dendrite structure of S4.

C. *Characterization*

Changes in cooling rate through the cross section of the samples affect the size and density of inclusions in various locations. Consequently, the characterization of inclusions must be based on images taken from at least three zones at the edge of the samples: one at the surface, another at 1/4 depth, and a third at 1/2 depth (see Figure 1(c)). In our study, each of the target zones was 200 μm wide. Samples that had previously been etched in 3 pct nital solution were imaged by a Scanning Electron Microscope (SEM, Hitachi SU1510/JSM-6700F). We counted the number of inclusions in 75 images, which had been taken continuously from each of the three zones. The chemical composition of inclusions was measured using the Energy Dispersive Spectrometer (EDS). The density of inclusions was calculated using the following equation:

$$N_A = n/s \qquad [2]$$

where n is the total number of detected inclusions, and s is the statistical area.

Vickers hardness tests were performed on all samples using a MH-5L microindenter with a load of 50 gf. In S4, which has a large variation in hardness among the three areas (as discussed in the results section), nanoindentation hardness was also measured using a G200 nanoindenter equipped with a Berkovich tip.

In preparation for the nanoindentation test, S4 was submerged in a solution of 80 pct $HClO_4$ and 20 pct glacial acetic acid at about 0 °C. While submerged, the sample was electro-polished at 40V for 15s. Once the sample was removed from the solution, it was cleaned ultrasonically.[29] The indentation sites that we selected were all in the interiors of grains. The maximum penetration depth was 2000 nm. Six indents were made at each depth. Nanoindentation hardness was determined by analyzing load-displacement (P-h) curves using the Oliver and Pharr method.[30]

For the Vickers test on all four samples, eight indentations were taken in each zone (see Figure 3). Vickers hardness values were expressed in GPa. Differences in hardness were statistically analyzed according to the T-test. If a P value in a T-Test was smaller than 0.01, the difference in hardness values was considered statistically significant.

Tensile tests were performed on three specimens taken from S4 (the sample with the highest hardness) using MTS CMT 5205 test machine at a rate of 0.12 mm/min. The strain was measured by cross-head reading because of the small specimen size (see Figure 4). Stress curve was plotted to show the yield strength, ultimate tensile strength and elongation of the specimens.

III. RESULTS AND DISCUSSION

In the following sections, a single-step DiCH method for making property-gradient low-carbon steels is described. The steels were made by casting to make the materials directly from the liquid metals, without any post-casting steps required. This DiCH method produced materials with very high ductility and with an ultra-hard layer at the surface. Desirable material properties were achieved by manipulating two variables: (1) free oxygen content before solidification, and (2) cooling rate during solidification.

A. *Influence of Oxygen Content and Cooling Rate on Inclusion Distribution*

The density of inclusions is influenced by both free oxygen content and cooling rate. As the solid/liquid interface advances from surface to center, free oxygen is forced to concentrate in the remaining zones. This concentration leads to the segregation of oxide inclusions in the center (1/2 depth). As cooling rate decreases from surface to center, nucleation rate also decreases. In other words, the remaining inclusions at center are larger in size but fewer in number. The distribution of oxides in DiCH samples is listed in Figure A1 in Appendix I. To describe the distribution of oxide

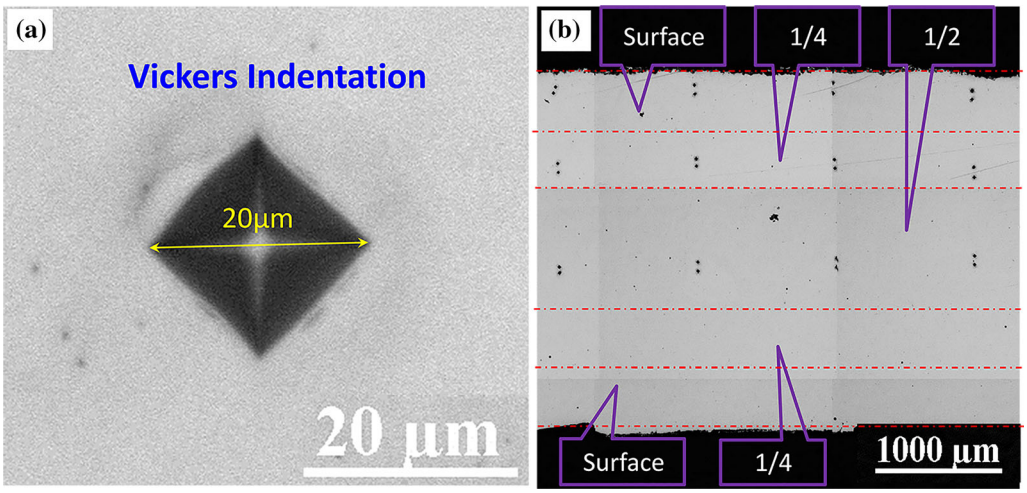

Fig. 3—Vickers indentation and locations. (*a*) Vickers indentation. Width and depth vary according to the hardness of the steel. (*b*) Location of indentations.

inclusions, we devised the term "particle density variation" (*PDV*), which is related to both free oxygen content ($[O]_s$) and cooling rate according to the following formula:

$$PDV = (PDC - PDS)/PDC \quad [3]$$

where *PDC* is Particle Density at Center, *i.e.,* 1/2 depth, and *PDS* is Particle Density at Surface (See Figures 5(a) and (b)). When [O]s is in the range of 25 to 45ppm and the cooling rate is higher than 550 K/s, the *PDV* is near zero and the distribution of inclusions is relatively uniform (see Figure 5(b)).

Samples S1 and S4 were both subjected to rapid cooling. Normally, such rapid cooling would inhibit excess segregation of oxygen in the center, but the oxygen content in S1, which was higher than in any other sample, actually negated this inhibition. Consequently, S1 had the greatest *PDV*; that is, the density of inclusions in the center (1/2 depth) was much higher than in the other two zones (see Figure 5(a)).

In S3, which had the lowest oxygen content and the slowest cooling rate, the *PDV* was almost as high as in S1, but for the opposite reason. Where oxygen content dominated in S1, resulting in oxide concentration at 1/2 depth, cooling rate dominated in S3, resulting in oxide concentration at surface. Consequently, neither S1 nor S3 produced even oxide distribution.

In both S2 and S4, the *PDV* was near zero (indicating an even distribution of oxides), but there is an important distinction to be made. Although both samples had similar oxygen content, the cooling rate of S4 was 4 times that of S2, so fast that the sample solidified within one second. The greater degree of undercooling that accompanied this rapid rate resulted in supersaturation, thus precipitating the simultaneous formation of a large number of very small oxides that were immediately trapped in the advancing solid/liquid interface. The result was an exceptionally high density of minuscule inclusions within a narrow size range. By contrast, the solid/liquid interface in S2, with its mediocre cooling rate, advanced much less rapidly, leaving time for some inclusions to grow larger than others. This resulted in a wide variety of sizes in S2, albeit with the same *PDV* as S4.

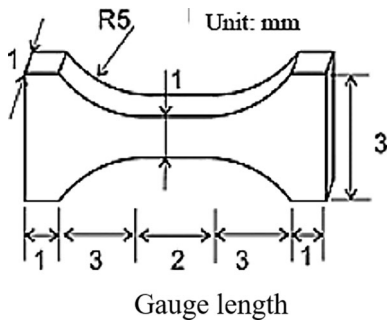

Fig. 4—Schematic illustration showing the size and shape of the tensile sample. Sample width was 1 mm and length was 2 mm.

B. *Effect of Inclusions on Microstructure*

Our low-carbon steel samples contained several morphologies: PF, Q-PF, martensite-like ferrite (MF, Appendix II), and AF. Of these morphologies, strength and hardness are usually highest and higher in steels containing MF and AF, respectively.[19]

Oxide inclusions containing Ti are known to act as nucleation sites for AF. The volume pct of AF varies depending on the number and size of those inclusions. The aim of this study is to determine the minimum number and optimum size necessary to achieve a consistently high volume pct of AF in as-cast steel.

Using SEM, we examined variations in microstructure along the cross section from surface to center in order to compare our four samples with respect to distribution of inclusions and morphology of microstructure. Samples S1 to S3 contained no desirable

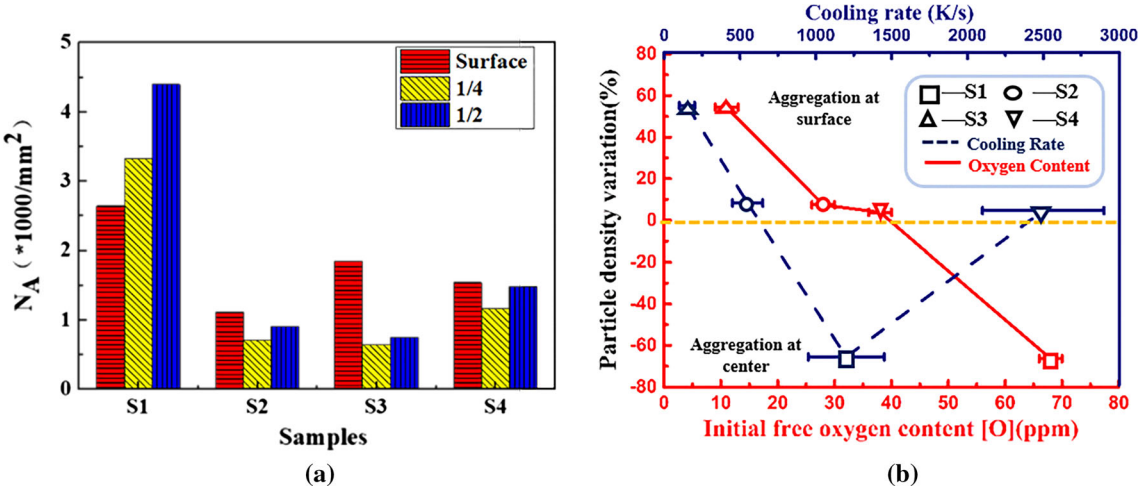

Fig. 5—Particle density and particle density variation in four samples: (*a*) Particle density (number per unit area) at surface, 1/4 depth, and 1/2 depth. (*b*) The effects of initial free oxygen content and cooling rate on inclusion distribution. Distribution is uniform when the value for particle density variation (PDV) is near 0. Positive PDV values indicate aggregation of inclusions toward the surface; negative values indicate aggregation toward the center.

phases for high hardness, but instead contained mainly either PF (in S1, Figures 6(a) through (c)), or Q-PF (for S2 and S3 Figures 6(d) through (i)).

In S4, two kinds of microstructure were observed, one fine and one coarse. Because of the coupling effect of initial free oxygen content (*i.e.*, 38 ppm) and cooling

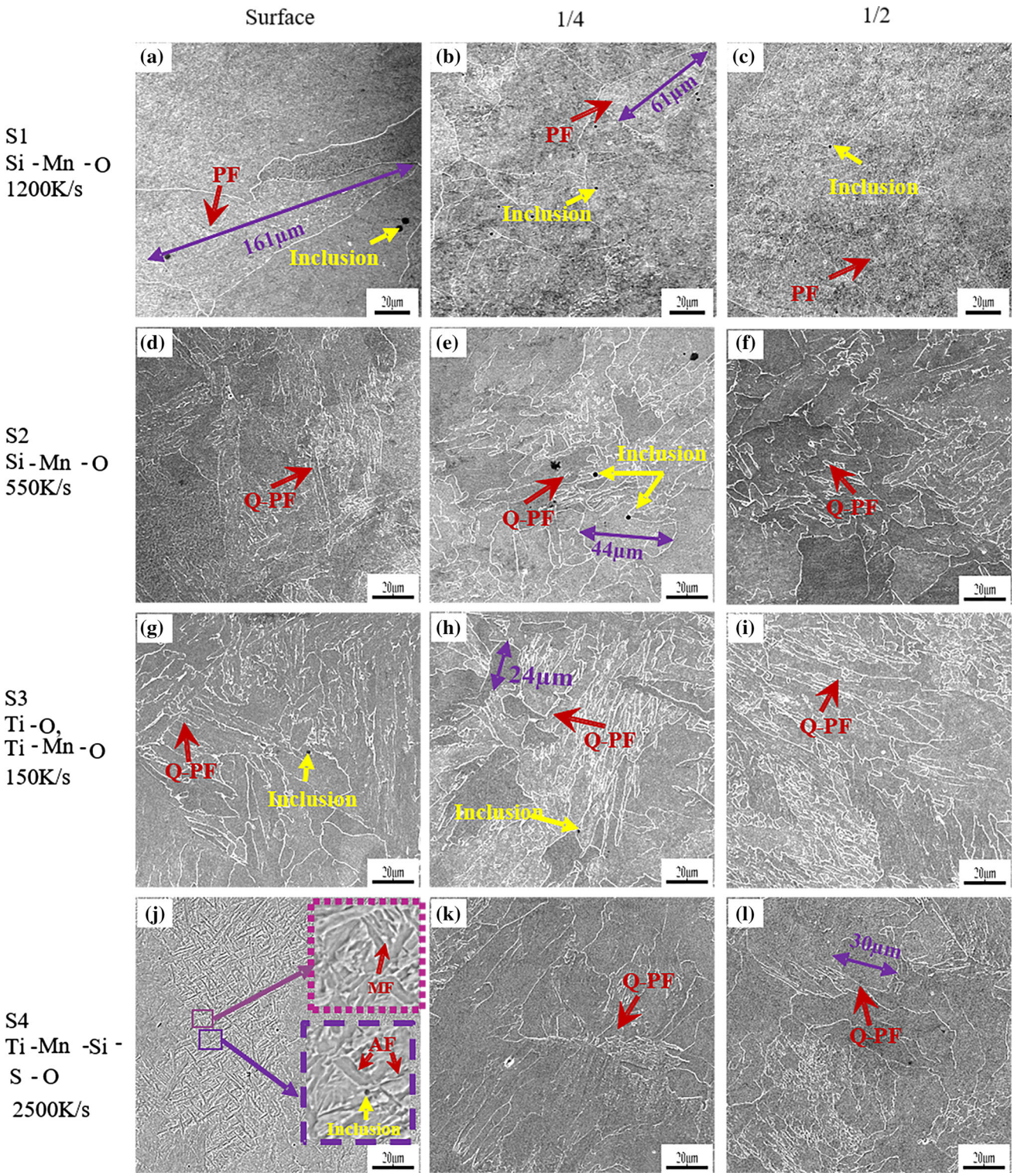

Fig. 6—Typical microstructure at surface, 1/4, and 1/2 depth of all four samples. Acicular ferrite (AF) nucleates on inclusions (yellow arrow in surface zone of S4) and has high-angle grain boundaries, giving it high hardness. Martensite-like ferrite (MF) has ultrafine grains with microstructure similar to that of martensite, which is known to be valuable for high hardness. Polygonal Ferrite (PF) and Quasi-Polygonal Ferrite (Q-PF) rank far below AF and MF in hardness. (*a–c*) In S1, PF grains are 70 μm wide at the surface, 67 μm at 1/4 depth, and 69 μm at 1/2 depth. (*d–i*) In S2 and S3, Q-PF grains are less than 30 μm in all three zones. (*j–l*) In S4, ultrafine AF and MF (0.5 to 1 μm wide) predominate at the surface, and small Q-PF grains (less than 30 μm) in the other two zones (Color figure online).

rate (*i.e.*, 2500 K/s), maximum refinement was achieved between 0 and 200 μm from the surface. The fine grains (0.5 to 1 μm wide), which occurred only near the surface, were composed of a high volume pct of AF and paralleled MF (Figure 6(j)). Coarser grains, which occurred mainly in the other two zones (1/4 and 1/2), were composed mainly of Q-PF (Figures 6(k) and (l)).

It has been established that PF and Q-PF nucleate mainly on austenite grain boundaries, while AF nucleates mainly on Ti-containing oxide inclusions within grains. The fact that only PF and Q-PF were found in S1 and S2 indicates that the inclusions presented in those samples did not contribute to the refinement of the microstructure (Figures 6(a) through (f)). This is because the inclusions in those samples were Mn-Si-O oxides rather than Ti-containing oxides (Figures 7(a) and (b)). Although Ti-containing oxides were detected in both S3 and S4 (Figures 7(c) and (d)), an appreciable volume pct of AF occurred only in S4. We speculate that only in S4 did the number and size of Ti-containing oxides pass the critical threshold for the formation of AF. Typical oxide inclusions in S4 were consisted of MnS and Ti_2O_3 (Figure 8). The selected area diffraction pattern (SADP) revealed that MnS had cubic structure (Figures 8(b) and (c)) and Ti_2O_3 hexagonal structure (Figures 8(d) through (f)). Researchers have found that when Ti_2O_3 and MnS occur together, they tend to be especially effective for AF nucleation.[20]

The composition of inclusions was more or less the same among the three zones of S4, but microstructure varied greatly from surface (where a high percentage of a mixture of AF and MF was detected) to center (where Q-PF was dominant). We investigated the size distribution of inclusions to determine the effect of their size and density on the formation of AF. We found that, at surface, the density of inclusions was higher in the 0.5 to 0.7 μm size range (about 600 per square millimeter) than at the other two depths of S4 (see Figure 9). All the inclusions located at the intersections of AF grain boundaries were in the size range of 0.5 to 0.7 μm. We concluded that (1) specific inclusions in the size range of 0.5 to 0.7 μm stimulated the nucleation of AF, and (2) when the density of such inclusions reached 600/mm^2, they contributed to a high volume pct of AF.

C. *Effect of Microstructure on Mechanical Properties*

Vickers hardness values were low in S1, S2, and S3 (from about 1.6 GPa to about 2.1 GPa). In S4, however, values were low only at 1/4 depth and 1/2 depth but rose to 4.2 GPa at surface (see Figure 10(a)). That value would be an incredibly high goal in the production of

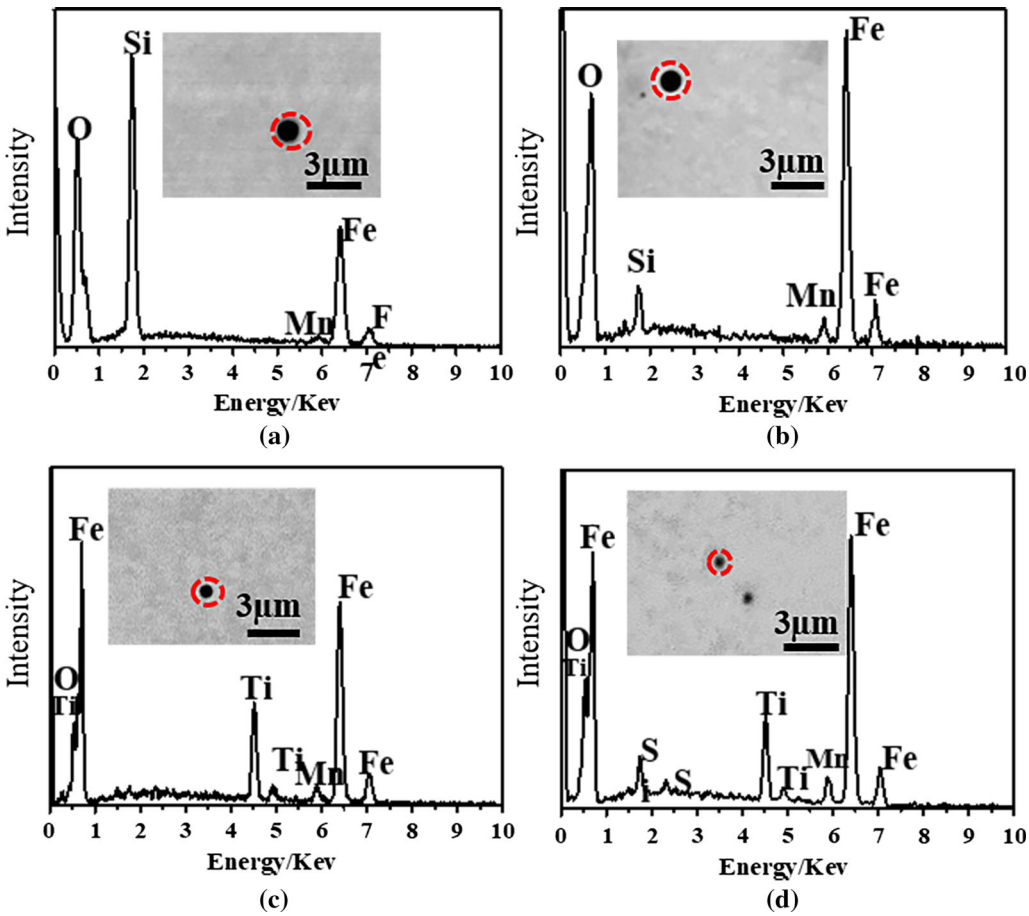

Fig. 7—Morphology and chemical composition of typical inclusions observed in the four samples: (*a*) S1, Si-Mn-O; (*b*) S2, Si-Mn-O; (*c*) S3, Ti-Mn-O; (*d*) S4, Si-Ti-Mn-O-S. The black dots in circles are the inclusions. The composition was analyzed by EDS.

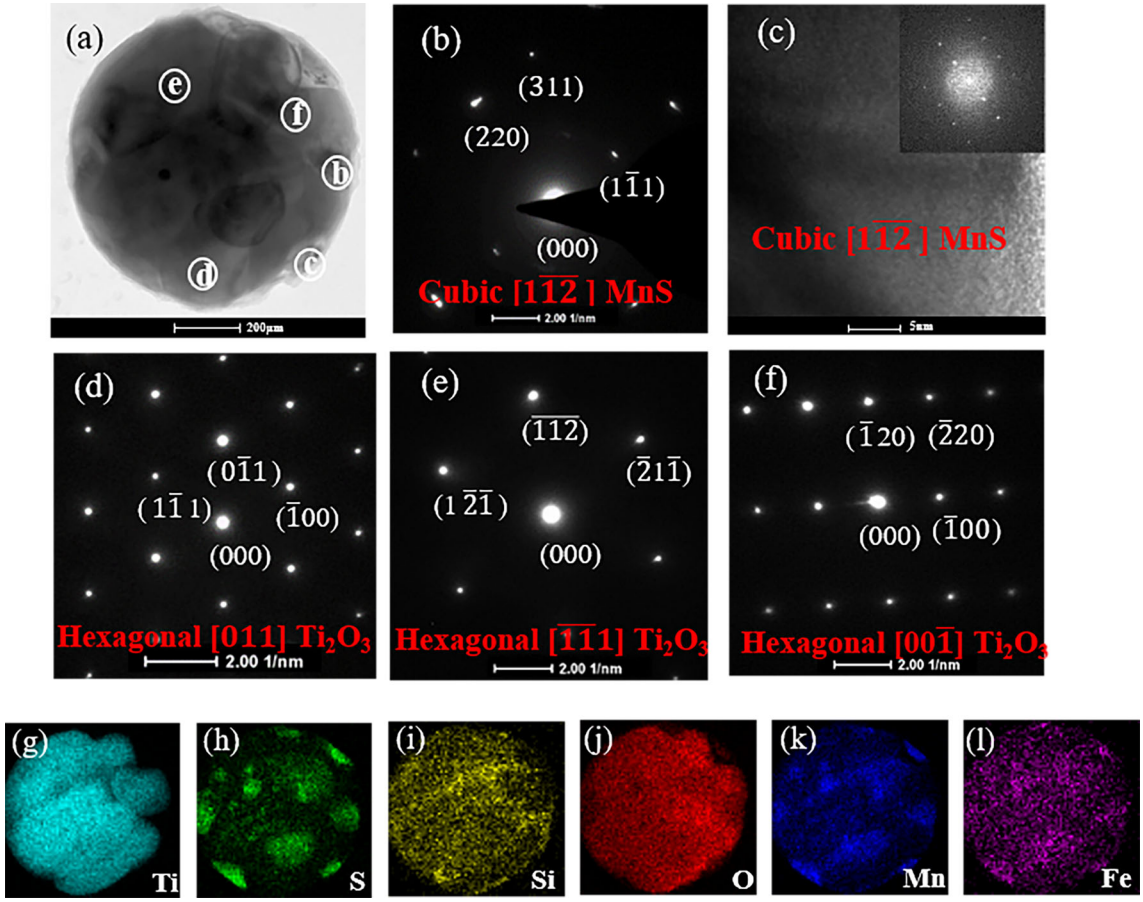

Fig. 8—Microscopy data of a typical composite oxide in S4. (*a*) TEM image. (*b*) to (*f*) SADP's obtained from areas b, c, d, e, and f in (*a*). (*g*) to (*l*) EDS mapping analysis of the oxide.

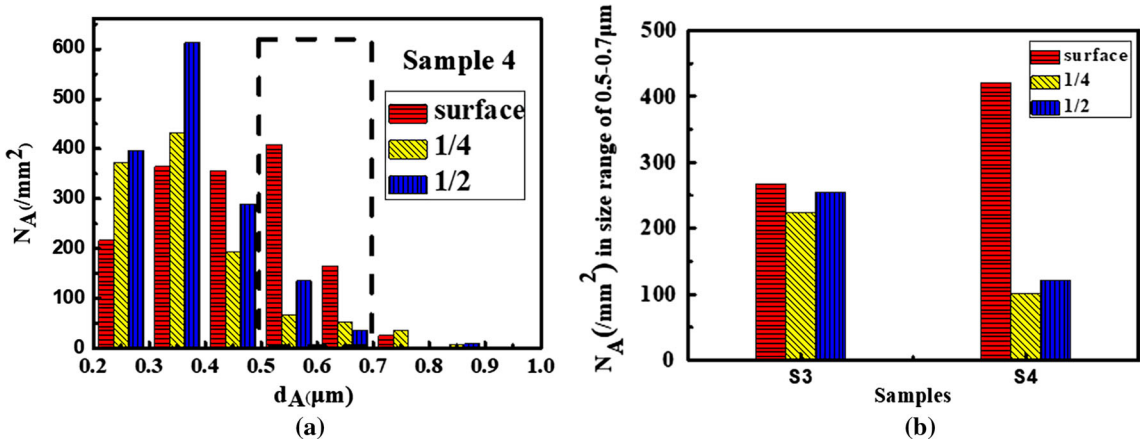

Fig. 9—Density of inclusions. (*a*) Distribution of inclusions in S4. Inclusions ranging from 0.5 to 0.7 μm are more plentiful at the surface than at the other two zones. (*b*) Comparison of S3 and S4. Inclusion density in the size range of 0.5 to 0.7 μm is significantly higher at the surface of S4 than in any other zone of either S3 or S4.

any low-carbon steel. Moreover, we achieved this high value without adding the costly steps of hot-rolling, cold-rolling, and quenching–the customary procedures for enhancing hardness and strength in steel production.

Variations in hardness can be explained by differences in the microstructure of the four samples. Hardness increases with decreasing grain size.[31] Some researchers stated that when grain size is finer, external force can be dispersed through more grains, resulting in reduced plastic deformation.[32] The size of the PF grains in S1 (the sample with the lowest hardness value) was greater than that of the Q-PF grains in S2, in S3, and in the 1/4 and 1/2 depth zones of S4 (see Figure 10(a)). By contrast, the microstructure in the surface zone of S4,

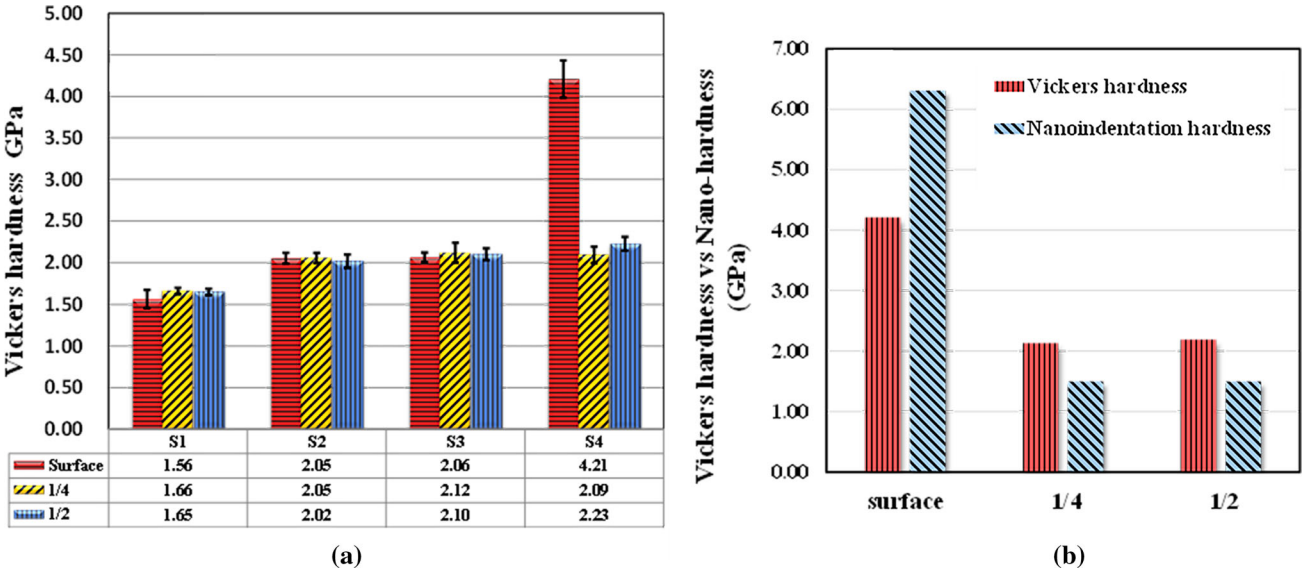

Fig. 10—Hardness measures. (*a*) Vickers hardness in each zone of the four samples. (*b*) Vickers hardness *vs* nanoindentation hardness of S4.

Table II. *P* Value for Significance Analysis of Hardness Between Different Samples

	S1 *vs* S2	S2 *vs* S3	S1 *vs* S4
Surface	0.01	0.68	0
¼	0	0.30	0
½	0	0.12	0

When $P \leq 0.01$, the difference in hardness is significant; otherwise, it is not significant.

Table III. *P* Value for Significance Analysis of Hardness Between Different Parts of Sample

	Surface *vs* 1/4	Surface *vs* 1/2
S1	0.02	0.08
S2	0.96	0.39
S3	0.37	0.24
S4	0	0

When $P \leq 0.01$, the difference in hardness is significant; otherwise, it is not significant.

which contained both AF and MF, was superfine, thus providing the exceptionally high hardness of that zone.

Because the difference in hardness between different areas is difficult to identify, T-test was performed to quantify the significance of the difference between different measurements. T-test results indicated significant differences in hardness between S1 and S2 and between S1 and S4, but the difference between S2 and S3 was insignificant (see Table II). The differences were significant between surface and 1/4 and between surface and 1/2 in S4 (see Table III), but the differences were insignificant between surface and 1/4 and between surface and 1/2 in S1, S2, and S3.

Nanoindentation hardness is usually higher than Vickers (microindentation) hardness. In the surface zone of S4, this was indeed true, but in the 1/4 and 1/2 depth zones of S4, nanoindentation hardness was actually slightly lower (see Figure 10(b)). The deformation zone during a Vickers hardness test is assumed to be 3 times the width of the microindentation. In our test, this width was 20 μm, so the deformation zone was about 60 μm on either side, or 120 μm in all. This was not only larger than the sample's grain size but also larger than its primary arm spacing (see Figures 2 and 6). Thus, at the 1/4 and 1/2 depth zones of S4, grain boundaries resisted deformation in the Vickers test, but not in the nanoindentation test. Since our nanoindentation tests were always performed inside grains, grain boundaries did not affect tests done at the 1/4 and 1/2 depths of S4, where grain size was larger than at the surface. Consequently, nanoindentation values were lower at the 1/4 and 1/2 depths. At the surface, however, because grain size was so fine that grain boundaries were necessarily involved regardless of the size of the indenter, the values for the nanoindentation test were higher, as expected.

The Vickers hardness in the surface zone of S4 reached 4.2GPa. Yield strength and ultimate tensile strength of S4 were 300 ± 11 and 370 ± 14 MPa, respectively (Figure 11(a)). The elongation was 32 ± 4 pct which is slightly smaller than the value (37 pct) of undeformed low-carbon steel showed in literature.[33] Close examination of the indentation produced in the Vickers hardness test revealed no cracks (Figures 11(b) through (c)). The edge of the indentation shows entire ductile deformation. This, along with the absence of cracks, indicates that the fracture toughness of the fine-grained region at the surface of S4 was very high.[34,35]

Hardness and yield strength are closely related to each other. They both measure the onset of plastic deformation. Yield strength in the surface zone of S4 can be related to Vickers hardness according to the following formula[36]:

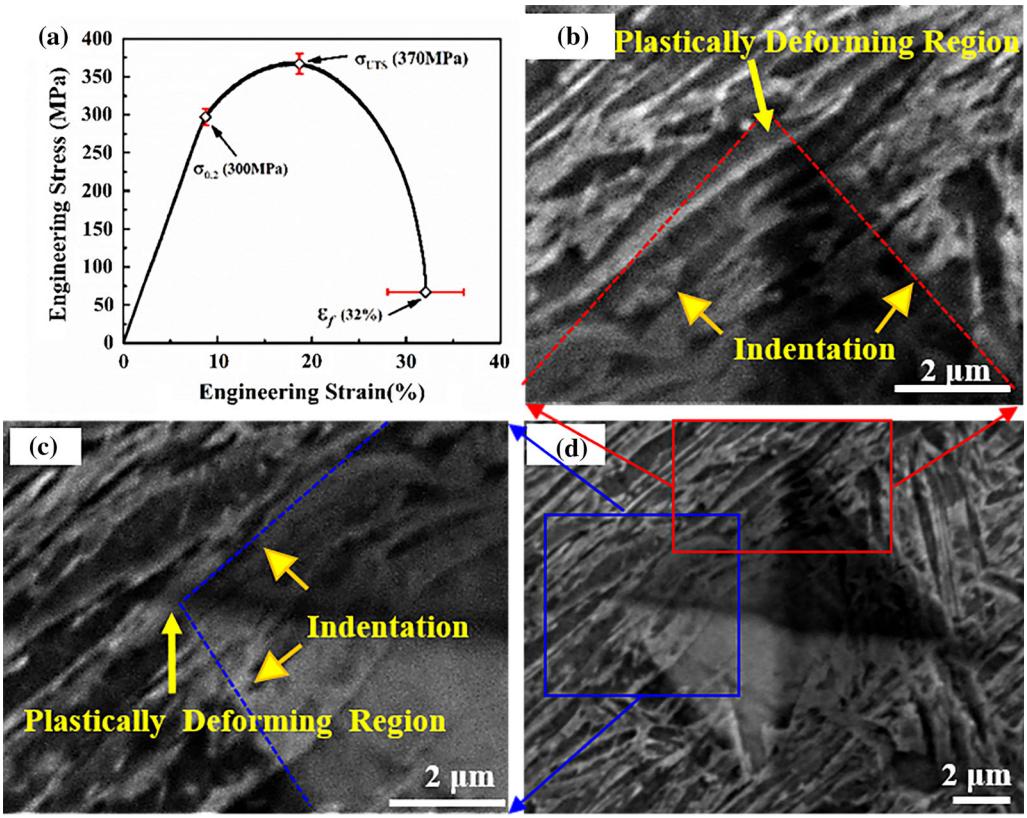

Fig. 11—Mechanical properties of S4 and SEM images of a typical Vickers hardness indentation at the surface of S4. (*a*) Engineering stress-strain curve of S4. (*b*) and (*c*) Partial enlargement of the indentation diagonal in (*d*) showing entire ductile deformation. (d) SEM image of Vickers hardness indentation (200 μm from the surface of S4).

$$H_0 = 4.15\sigma_y \qquad [4]$$

where σ_y is yield strength and H_0 is hardness. The coefficient (4.15) is very close to data previously obtained in research on pearlitic steels.[37] The yield strength value in the surface zone of S4 was calculated at > 1.0 GPa, which was 2 times as high as that of the other samples.

IV. CONCLUSIONS

A single-step DiCH method for making property-gradient low-carbon steels was developed by using the casting process itself to make the materials directly from the liquid metals, without any post-casting steps required. This DiCH method produced materials with high strength and with an ultra-hard layer at the surface. Desirable material properties were achieved by manipulating two variables: (1) free oxygen content before solidification, and (2) cooling rate during solidification.

Inclusions tended to remain smaller than 1 μm when the cooling rate was higher than 150K/s. The distribution of inclusions was relatively uniform when free oxygen content was in the range of 25 to 45 ppm and cooling rate was higher than 550 K/s.

Multi-component, Ti-containing oxides in the size range of 0.5 to 0.7 μm served as nucleation sites for AF. A high percentage of AF was formed when the density of the inclusions in this size range increased to 600/mm^2.

In the sample containing some MF along with a large amount of AF, both strength and hardness reached high values. The ultimate tensile strength was 370 $\pm$ 14 MPa. Vickers hardness at 200 μm from the surface of S4 reached 4.2 GPa, about 2 times as high as other samples containing mainly PF and Q-PF.

ACKNOWLEDGMENTS

This work was supported by the National Natural Science Foundation of China (No. U1460103). Support was also provided by the Instrumental Analysis & Research Center in Shanghai University. The manuscript was finalized when Dr. Li worked as a visiting scholar at the National High Magnetic Field Laboratory, which is supported by NSF DMR-1157490, the State of Florida, and DOE. Our thanks to Dr. Mary Tyler for editing.

APPENDIX I: SEM IMAGES OF INCLUSION DISTRIBUTION IN ALL FOUR SAMPLES

See Figure A1.

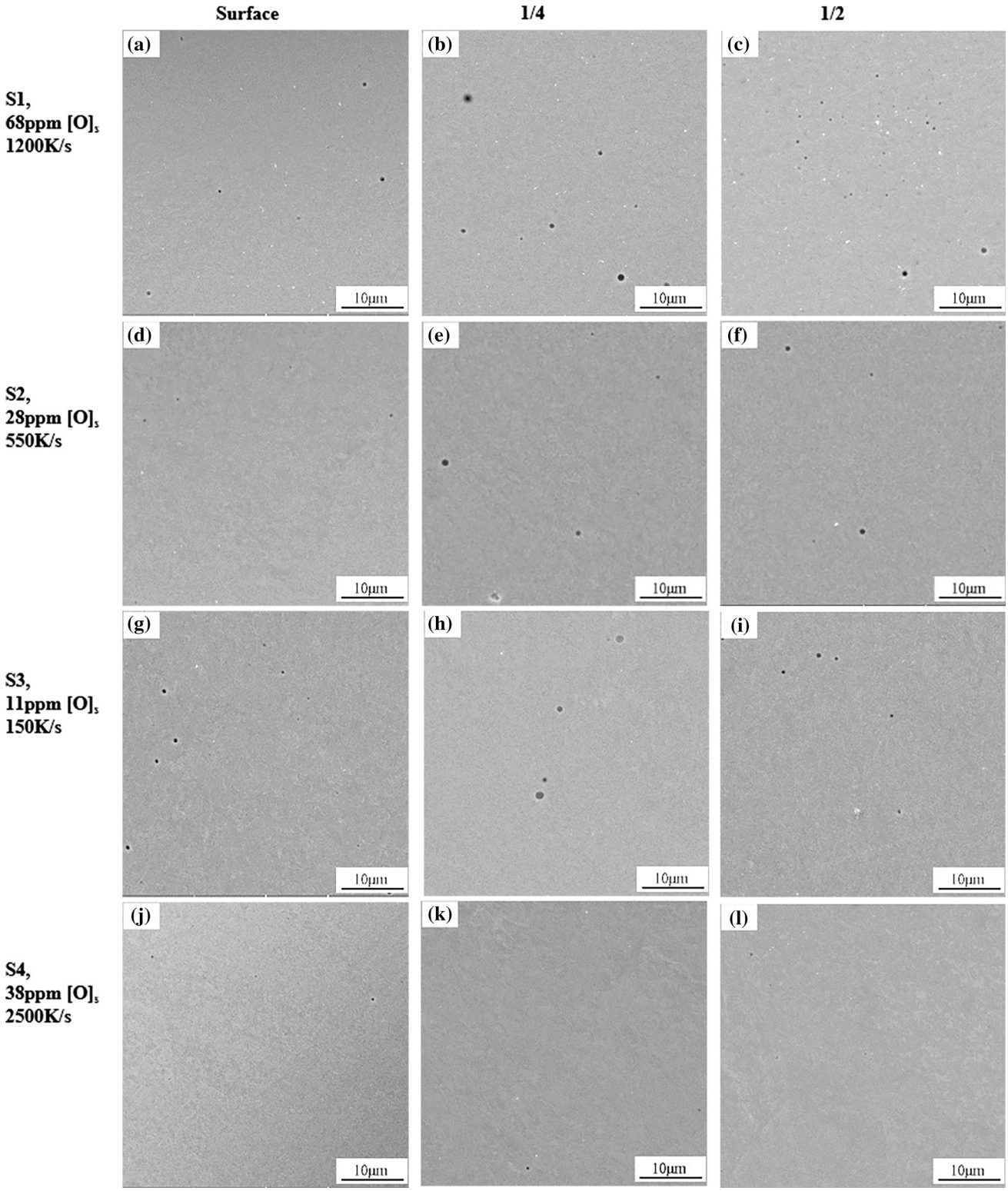

Fig. AI—SEM images showing distributions of inclusions in surface, 1/4 depth, and 1/2 depth zones of all four samples. Free oxygen contents and cooling rates are listed on left. The dark dots are inclusions and the white dots are impurities. (*a* through *c*) The distributions of inclusions in surface, 1/4 depth, and 1/2 depth zones of S1. (*d* through *f*) The distributions of inclusions in surface, 1/4 depth, and 1/2 depth zones of S2. (*g* through *i*) The distributions of inclusions in surface, 1/4 depth, and 1/2 depth zones of S3. (*j* through *l*) The distributions of inclusions in surface, 1/4 depth, and 1/2 depth zones of S4.

APPENDIX II: ABBREVIATIONS USED TO DESCRIBE FERRITE AND MARTENSITE MORPHOLOGIES

- PF, polygonal ferrite, refers to roughly equiaxed grains with straight boundaries and no substructure.[38]
- Q-PF, quasi-polygonal ferrite, refers to grains with undulating boundaries, which might cross prior austenite boundaries containing a sub-structure.[38]
- AF, acicular ferrite, refers to a microstructure with high-angle boundaries and randomly oriented needle-shaped lenticular plates.[39]
- MF, martensite-like ferrite, has ultrafine grains with microstructure similar to that of martensite, which is known to have high hardness.

REFERENCES

1. D.J. Sosinsky, P. Campbell, R. Mahapatra, W. Blejde, and F. Fisher: *Metallurgist*, 2008, vol. 52, pp. 691–99.
2. S.L. Shrestha, K.Y. Xie, C. Zhu, S.P. Ringer, and C. Killmore: *Mater. Sci. Eng. A*, 2013, vol. 568, pp. 88–95.
3. Z.Z. Wang, K. Carpenter, Z.X. Chen, and C. Killmore: *Mater. Sci. Eng. A*, 2017, vol. 700, pp. 234–40.
4. W.L. Costin, O. Lavigne, and A. Kotousov: *Mater. Sci. Eng. A*, 2016, vol. 663, pp. 193–203.
5. D.V. Doane and J.S. Kirkaldy: *Hardenability concepts with applications to steel*, 1st ed., Metall. Soc. AIME, Chicago, 1978, p. 229.
6. G. Krauss: *Mater. Sci. Eng. A*, 1999, vols. 273–275 (99), pp. 40–57.
7. H.F. Wang and F. Xia: *Iron*, 1984, vol. 10, pp. 39–44.
8. C.F. Wang, M.Q. Wang, J. Shi, W.J. Hui, and H. Dong: *Iron Steel*, 2007, vol. 42 (11), pp. 57–60.
9. H. Ohta and H. Suito: *ISIJ Int.*, 2006, vol. 46 (1), pp. 42–49.
10. H. Goto, K. Miyazawa, K. Yamaguchi, S. Ogibayashi, and K. Tanaka: *ISIJ Int.*, 1994, vol. 34 (5), pp. 414–19.
11. H. Yu and J. Li: *Int. J. Miner. Metall. Mater.*, 2015, vol. 22 (11), pp. 1157–62.
12. L.Q. Deng, S.L. Zou, D.W. Tang, Y.P. Xie, and D. Zhang: *Cast. Technol. Chin.*, 2016, vol. 9, pp. 1807–11.
13. D.J. Sosinsky, P. Campbell, R. Mahapatra, W. Blejde, and F. Fisher: *Metallurgist*, 2008, vol. 52 (11–12), pp. 691–99.
14. Z.P. Xiong, A.G. Kostryzhev, and N.E. Stanford: *Mater. Sci. Eng. A*, 2016, vol. 651, pp. 291–305.
15. S. Ge, S. Chang, T. Wang, L.E. Calzado, and M. Isac: *Trans. Iron Steel Inst. Jpn.*, 2014, vol. 54 (3), pp. 1–12.
16. J.S. Byun, J.H. Shim, J.Y. Suh, Y.J. Oh, and Y.W. Cho: *Mater. Sci. Eng. A*, 2001, vols. s 319–321(00), pp. 326–31.
17. C.R. Killmore, A. Phillips, H. Creely, H. Kaul, and P. Campbell: *Iron Steel Technol.*, 2007, vol. 10 (10), p. 90.
18. H.T. Liu, Z.Y. Liu, Y.Q. Qiu, and G.M. Cao: *Mater. Charact.*, 2009, vol. 60 (1), pp. 79–82.
19. D.S. Sarma, A.V. Karasev, and P.G. Jonsson: *Trans. Iron Steel Inst. Jpn.*, 2009, vol. 49 (7), pp. 1063–74.
20. J.S. Byun, J.H. Shim, Y.W. Cho, and D.N. Lee: *Acta Mater.*, 2003, vol. 51 (6), pp. 1593–1606.
21. S. St-Laurent: *Mater. Sci. Eng. A*, 1992, vol. 149 (2), pp. 203–16.
22. W. Mu, H. Mao, H. Jonsson, and K. Nakajima: *Steel Res. Int.*, 2016, vol. 87 (3), pp. 311–19.
23. D. Loder, S.K. Michelic, and C. Bernhard: *J. Mater. Sci. Res.*, 2017, vol. 6 (1), pp. 24–43.
24. Z. Xiong, S. Liu, X. Wang, C. Shang, and R.D.K. Misra: *Mater. Charact.*, 2015, vol. 106, pp. 232–39.
25. Y. Li, X.L. Wan, W.Y. Lu, A.A. Shirzadi, and O. Isayev: *Mater. Sci. Eng. A*, 2016, vol. 659, pp. 179–87.
26. Z. Zhang and R.A. Farrar: *Mater. Sci. Technol.*, 1996, vol. 12 (3), pp. 237–60.
27. B. Kim, S. Uhm, C. Lee, J. Lee, and Y. An: *J. Eng. Mater. Technol.*, 2005, vol. 127 (2), pp. 204–13.
28. A. Suzuki, T. Suzuki, Y. Nagaoka, and Y. Iwata: *J. Jpn. Inst. Met.*, 1968, vol. 32 (12), pp. 1301–05.
29. H.F. Huang, J. Li, D.H. Li, R.D. Liu, and G.H. Lei: *J. Nucl. Mater.*, 2014, vol. 454 (1–3), pp. 168–72.
30. W.C. Oliver and G.M. Pharr: *J. Mater. Res.*, 2004, vol. 19 (1), pp. 3–20.
31. E. O. Hall: *Proceedings of the Physical Society*, 2002, vol. 64(6), p. 495.
32. H. Huang, C. Yang, M.D.L. Reyes, Y. Zhou, and L. Yan: *J. Mater. Sci. Technol.*, 2015, vol. 31 (9), pp. 923–29.
33. L. Hao, N. Xiao, C. Zheng, and D. Li: *J. Mater. Sci. Technol.*, 2010, vol. 26 (12), pp. 1107–13.
34. W. Vandermeulen, R.W. Bosch, and F. Snijkers: *J. Mater. Sci.*, 2015, vol. 50 (7), pp. 2932–43.
35. E. Breval, G.C. Dodds, and N.H. Macmillan: *Mater. Res. Bull.*, 1985, vol. 20 (4), pp. 413–29.
36. M. Dao, N. Chollacoop, K.J.V. Vliet, T.A. Venkatesh, and S. Suresh: *Acta Mater.*, 2001, vol. 49 (19), pp. 3899–3918.
37. K. Han, D.V. Edmonds, and G.D.W. Smith: *Metall. Mater. Trans. A*, 2001, vol. 32 (6), pp. 1313–24.
38. P. Cizek, B.P. Wynne, C.H.J. Davies, B.C. Muddle, and P.D. Hodgson: *Metall. Mater. Trans. A*, 2002, vol. 33 (5), pp. 1331–49.
39. D. Loder, S.K. Michelic, and C. Bernhard: *J. Mater. Sci. Res.*, 2017, vol. 6 (1), pp. 24–43.